ChemElectroChem

Chemistry Europe
European Chemical Societies Publishing

Accepted Article

Title: Spatially Resolved Electron Transport through Anode-Respiring Geobacter sulfurreducens Biofilms: Controls and Constraints

Authors: Xiaojia He, Grayson Chadwick, Fernanda Jiménez Otero, Victoria Orphan, and Christof Meile

To be cited as: *ChemElectroChem* 10.1002/celc.202100111

Link to VoR: https://doi.org/10.1002/celc.202100111

WILEY-VCH

WILEY-VCH

FULL PAPER

Spatially Resolved Electron Transport through Anode-Respiring *Geobacter sulfurreducens* Biofilms: Controls and Constraints

Xiaojia He,*[a] Grayson Chadwick,[b] Fernanda Jiménez Otero,[c] Victoria Orphan [b] and Christof Meile [a]

[a] Dr. X. He, Prof. Dr. C. Meile
Department of Marine Sciences
University of Georgia
Athens, GA, USA.
E-mail: xiaojia.he@hotmail.com, xiaojia.he@emory.edu
[b] Dr. G. Chadwick, Prof. Dr. V. Orphan
Division of Geological and Planetary Sciences
California Institute of Technology
Pasadena, CA, USA
[c] Dr. F. Jiménez Otero
College of Biological Sciences
George Mason University
Fairfax, VA, USA

Supporting information for this article is given via a link at the end of the document.

Abstract: Microbial fuel cells (MFCs) with *Geobacter sulfurreducens* have been shown to produce high current densities; however, electron transport in *G. sulfurreducens* biofilms is not fully understood. Here, we utilize a spatially resolved numerical model describing this electron transfer to constrain mechanisms and controls on metabolic activity. Our model reproduces the metabolic activity profile obtained using nanoSIMS under positive (+0.24V SHE) and negative (-0.1V SHE) anode potentials. The simulations indicate that the distribution of the electric potential and pH both control cellular metabolism. Model simulations reproducing the experimentally determined activity patterns also support the presence of two activity modes in *G. sulfurreducens* biofilms, with a shift from a redox mid-potential of -0.07V SHE to -0.15V SHE. Our model provides valuable insights into the fundamental mechanisms of electron transfer at Micron-scale in conductive biofilms which can inform MFCs designs that maximize current production by minimizing the impact of inhibitory factors.

Introduction

Extracellular electron transfer (EET) in microbial systems can be carried out through the transport of chemical substances (mediated electron transfer) or by electron flow (direct electron transfer, DET) via physical contact using outer surface c-type cytochromes,[1] electrically conductive pili[2] or a matrix of extracellular polymeric substances.[3-5] DET is potentially much more efficient than mediated EET, and effective over long distances[6]. As such, microorganisms capable of DET have attracted attention in the fields of microbial physiology, microbial ecology, and biotechnology[7-9], where understanding the EET mechanisms in current generating biofilms on electrodes in microbial fuel cells (MFCs) and the factors controlling their metabolic rates is important for the optimization of practical applications and a better understanding of natural and/or industrial systems as the functioning EET components such as conductive filaments (e.g. pili) may enhance cellular respiratory activities and viability and can be exploited to design effective *in situ* bioremediation strategies.[10]

Geobacter sulfurreducens, one of the best studied model organisms carrying out DET, can produce high current densities in MFCs in which the anode serves as the terminal electron acceptor[11, 12]. There are two main proposed mechanisms underlying direct EET, a hotly debated topic for *G. sulfurreducens* (e.g. [13-15] and [16-19]): 1). Metal-like conduction and 2). Electron hopping. Metal-like conduction is characterized by the presence of free-moving valence electrons. This is usually realized by forming a conjugated system in which π-orbitals overlap with one another in a chain of molecules [20]. Measurements on individual pili from *G. sulfurreducens* showed high conductivities of approximately 50 mS cm^{-1} at pH 7 [21], with a temperature and pH dependent conductivity response [21, 22]. Several studies indicated that closely packed aromatic amino acids on pili may give rise to such metal-like conductivity[23, 24]. In contrast, electron hopping is a phenomenon where electrons are localized on a chain of redox active molecules, and are transferred in a multistep bucket-brigade manner[25]. Redox proteins such as Ru-modified azurin and cytochromes can have long-range electron hopping over 20 Å [26, 27], electron hopping has been observed between aromatic side chains of peptides [28, 29], and was suggested to be responsible for electron transfer through filament-associated multiheme c-type cytochromes [14, 30]. A recent report showed that *G. sulfurreducens* conductive filaments were assembled by hexaheme cytochrome OmcS, with a tight packing distance at 3.5–6 Å over a micrometer length [31], corroborated by interatomic distances between adjacent porphyrins of the hexaheme cytochrome at 4.1 Å or less [32]. Moreover, the polymerization of monomeric cytochromes (e.g. OmcZ) could further reduce the heme-heme distance[33]. At such closely packed distance, multistep electron hopping along the conductive filaments thus are made possible (< 20 Å [26, 27]). ~~While~~ Acknowledging that many scientists possess strikingly different perspectives on this particular matter[19], we refer the reader to the literature for arguments for metal-like conductivity[18, 21-24] and those supporting electron hopping[34-42].

The anode potential regulates metabolism, electrochemical respiration and anabolic activity in *G. sulfurreducens* biofilms.[43-46] Understanding how *G. sulfurreducens* produces high current densities, and what ultimately is responsible for limiting this process motivates the development of a reactive transport model. Such models account for the fundamental physics and chemistry in natural systems and can quantitatively integrate microbiological insights into an environmental context[47]. For example, considering soluble electron shuttles, Picioreanu et al. (2010)[48] simulated pH dynamics and the evolution of current density in electroactive and fermentative biofilms on electrodes over time. Marcus et al. (2007)[49] and Torres et al. (2008)[50] showed that EET in *G. sulfurreducens* biofilms can be limited by biofilm conductivity, electron donor flux and local potential. The distinction between these mechanisms is important, as it affects potential losses and current densities in biofilms grown on electrodes (see Torres et al. (2010)[51] for a review of different extracellular electron transfer mechanisms). Korth and Harnisch (2019)[52] recently presented a model of direct EET that demonstrates that energy harvest not only depends on anode potential but can be determined by intracellular conditions. Thus, earlier studies showed that both pH[53-55] and electric potential dependencies[42-46, 56, 57] shape cell activity within biofilms. However, until recently, no robust, direct, and spatially resolved cell activity data was available. A recent study identified for the first time the stratification of active cell layers within *G. sulfurreducens* biofilms where even under ideal conditions (i.e. non-limiting concentrations of buffer and nutrients and anodes poised at favorable redox potential) the highest anabolic activity is found in cell layers closest to the electrode and decreases linearly in cell layers further from the electrode [58]. Here, we build on prior models of biofilm activity by using spatially resolved cell activity data [58] enabling the integration of the effect of extracellular electron transport, physiological adaptations and energetic and chemical feedbacks into our model.

The model we present here adopts electron hopping as the underlying mechanism, consistent with the observed drop in redox potential with increasing distance from the anode surface in electroactive *G. sulfurreducens* biofilms [59] and – as shown below – is in line with the first direct measurement of spatially resolved anabolic activity in *G. sulfurreducens* biofilms during anode-respiring conditions [58]. Recent data collected using stable isotope probing coupled to nanoSIMS revealed distinct metabolic activity stratifications in anode-respiring *G. sulfurreducens* biofilms under two different anode redox potentials[58]. These unique experimental results provide significant constraints on reaction transport models of EET, enabling us to identify the controls on current production with relevance to the functioning of MFCs.

Results and Discussion

Spatial resolution on metabolic activity

Our simulations reproduced the distinct metabolic profiles in *G. sulfurreducens* biofilms under two different anode electric potentials (Figure 1). The model shows that *G. sulfurreducens* were most active close to the electrode surface for both high and low anode electric potentials, with maximum cell-specific activity approximately at 30 fmol acetate cell^{-1} day^{-1} near the electrode, comparable to the value measured independently under similar experimental conditions[60]. At more positive anode electric potential (+0.24 V; all potentials presented in this study are with respect to standard hydrogen electrode, abbreviated as SHE), two metabolic activity peaks were observed at a distance ~2 µm and ~12 µm away from the anode surface, respectively. Metabolic activity was slightly reduced at the anode surface, whereas no such effect was observed for simulations under more negative anode potential (-0.1V). In agreement with the experimental data, model simulations with low anode potential yield metabolic activity in *G. sulfurreducens* biofilms approaching zero at a distance >10 µm from the electrode, with no secondary peak in activity. The first 5 µm biofilms closest to the electrode surface contributed approximately 61% and 79% of the total current density of the *G. sulfurreducens* biofilms at high and low anode potential, respectively (Fig. 1B), with 83% and 98% of the current being produced within 10 µm of the anode and >98% and 100% of all production originating from within 15 µm (Fig. 1B). Our findings are consistent with earlier experimental studies showing that maximum *G. sulfurreducens* biofilm activity was reached with a biofilm thickness of ~20 µm[61], and addition of new biomass fails to proportionally increase total current[58, 61, 62], likely due to cell lysis or consumption of cellular material in outer layers of the long-term, thicker biofilm[58].

These model results emerge from the integrated effect of microbial, chemical and physical factors, with microbial activity depending on pH and redox state of the local environment, (expressed by the factors F_{pH} and F_e, respectively, which vary between 0 and 1, quantifying the extent of inhibition), the bacterial phenotype (reflected in midpoint potential of redox molecules involved in DET) and availability of reactants.

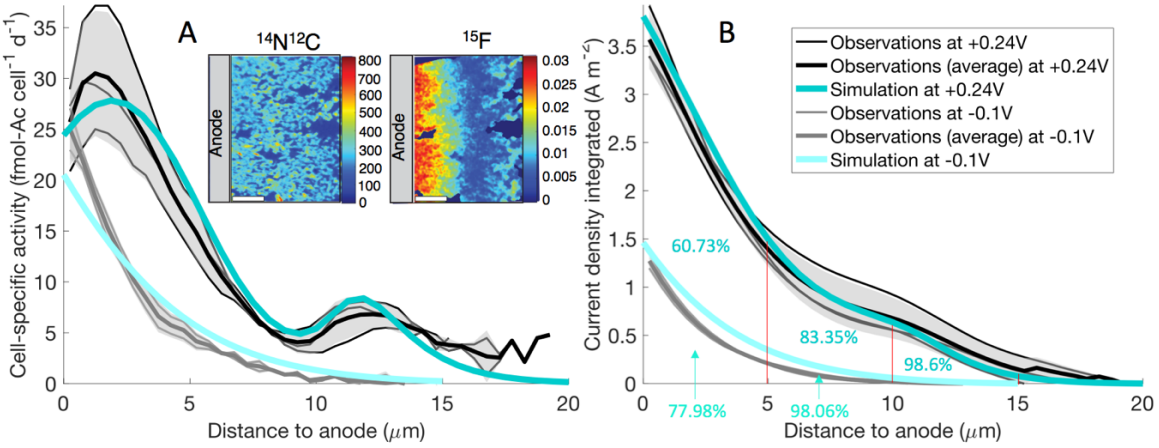

Figure 1. Model validation of distance dependent cell specific activity profiles using ^{15}N measurements by nanoSIMS at high (+0.24 V) and low (-0.1 V) anode potentials (A). (B) shows current density integrated over biofilm thickness and the cumulative contribution at every 5 μm. Average ^{15}N incorporation values for three biological replicates for the high potential condition and two biological replicates for low potential conditions. Experimental data is binned in half-micron increments from the electrode surface and recast into metabolic rates using Eq.(2). Modeling results (blue lines) are binned in a similar way for direct comparison. Inset: a characteristic nanoSIMS image from a biofilm grown at +0.24 V oriented with anode on the left side, bulk media on the right. The $^{14}N^{12}C^-$ image shows the extent of the biofilm, while ^{15}F fractional abundance of ^{15}N ($^{15}F = {}^{15}N^{12}C/({}^{14}N^{12}C+{}^{15}N^{12}C)$) reveals both a major peak of isotope incorporation at the biofilm-anode interface and a secondary peak in activity near the biofilm surface. The horizontal white scale bar corresponds to 5μm.

Potential losses are the dominant factor shaping the distribution of metabolic activity

Reduced microbial activity with increasing distance from the anode surface is the dominant trend in both experimental data and modeling results (Figure 1), and this pattern is driven by the decreasing electric potential (ϕ_{net}) (Figure 2A&B). Two factors, activation loss (ϕ_{act}) and ohmic resistance loss (ϕ_{om}), contribute in different ways to this potential loss, preventing *G. sulfurreducens* from experiencing the poised anode potential (ϕ_{anode}) throughout the biofilm. Activation losses incur in the charge transfer of electrochemical reactions[14, 63], such as the transfer of electrons on the conductive biofilms ($Cyt_{red} \rightleftharpoons Cyt_{ox} + e^-$), and from the biofilm onto the electrode (Rxn 2). The ohmic loss results from the electronic resistance on biofilms and at the electrode surface. The combined effect of these losses is that at the anode surface, *G. sulfurreducens* cells experienced an electric potential ~0 V and ~-0.17 V for simulations with the anode poised at +0.24 V and -0.1V, respectively. Activation loss dominated near the electrode surface, while ohmic resistance was the main loss term further away from the anode (> 6 μm at high, > 4 μm at low anode potential; Figure 2). Together, these losses reduce the electric potential experienced by cells in a linear fashion with distance from the anode. This causes the decrease in metabolic activity away from the electrode surface as quantified by the potential constraint (F_θ) (Figure 2).

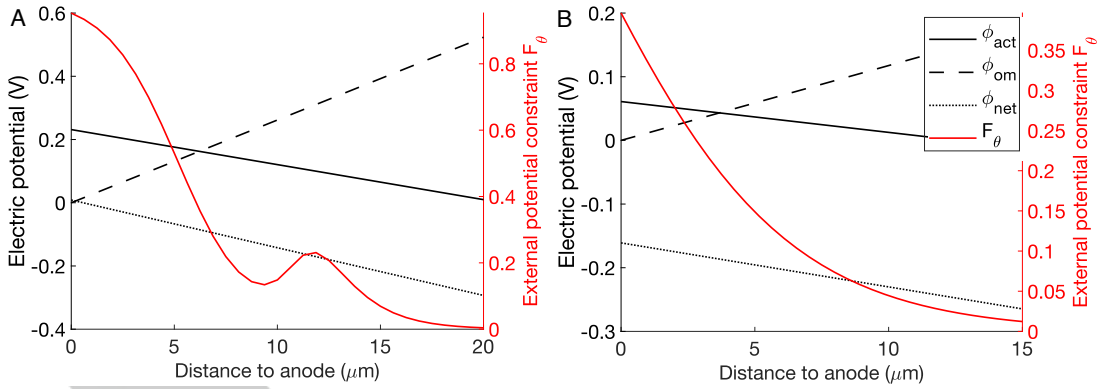

Figure 2. The modeled effects of activation (ϕ_{act}) and ohmic resistance (ϕ_{om}) losses on net effective electric potential (ϕ_{net}) through the biofilm, and the resulting potential constraints on metabolic activity (F_θ) in red. A and B represent model results for more positive (+0.24 V) and more negative (-0.1 V) anode potentials, respectively.

A secondary metabolic peak arises from redox centers with different midpoint potentials

A secondary metabolic peak at a distance > 10 μm from the electrode surface was consistently observed for *G.*

sulfurreducens biofilms under high anode potential [58]. Our model reproduced this feature of the metabolic activity profile (Figure 1), and the pattern arises from the potential constraint F_e (Figure 2A). This second peak observed in the model is caused by switch in the redox center mid-potential $\emptyset^{0'}_{\frac{Ox}{Red}}$ from -0.07 V to -0.15 V, which occurs at a distance of ~10 μm from the electrode where the effective electrical potential (ϕ_{net}) crosses the critical potential (ϕ_c). It is noted that the switching function between different redox centers embedded in potential constraint F_e (Eq. 7) is based on actual experimental determination that there are high and low potential systems in *G. sulfurreducens* biofilms[64]. No secondary peak occurs in biofilms simulated at low anode potential (Figure 2B), because ϕ_{net} at the anode surface is already below ϕ_c, and therefore the entire biofilm is utilizing the lower potential redox center.

pH effects on metabolic activity near the anode surface

A feature of the metabolic activity pattern not explained by potential losses and redox center switching is the slight decrease in activity observed at the anode surface in *G. sulfurreducens* biofilms grown at +0.24 V (Figure 1). Simulations show that due to the overall higher metabolic rates, *G. sulfurreducens* grown at high anode potentials experienced a stronger pH gradient than those at low potential, with pH values at the anode of ~6.15 and ~6.45 at high and low anode potential, respectively (Figure S3). Notably, earlier work suggested that proton transport can be the limiting factor for the current density produced by electroactive biofilms[48, 65]. Korth et al. (2015)[66] also reported a model framework that simulated the pH gradient with depth in a *Geobacter* biofilm, which is consistent with our model predications, but lacks the ability to link this gradient to the observed metabolic stratification and did not provide spatially resolved metabolic activity. In our current model, we attribute the decrease of the simulated metabolic activity near the anode surface at high anode potential to this difference in pH, and this is reflected in the model by the decrease in F_{pH} as pH approaches and falls below the threshold C_{pH} (Figure S3A & B).

To better understand the role of pH in shaping biofilm activity we numerically examined the effect of varying experimental conditions and biological model parameters. Lowering C_{pH} eliminates the decrease in metabolic activity at the anode surface (see Figure S6). Conversely, increasing C_{pH} causes a more intense drop in F_{pH} that begins further out in the biofilm, leading to more severe growth inhibition at the anode surface and shifting the first metabolic activity peak farther away from the anode (Figure S6). We can exclude the possibility that the low metabolic activity was caused by the limited diffusion of substrate to the biofilm, as demonstrated by the high simulated acetate concentrations throughout the biofilm (Figure S7) and the previously acquired experimental data from thick *G. sulfurreducens* biofilms.[58]

pH inhibition depends on both the pH buffering capacity and the level of metabolic activity. A reduced pH buffering capacity, modeled here by lowering the HCO_3^- concentration in solution, can significantly limit the removal of H^+ and subsequently inhibit the metabolic activity in the inner biofilm layer, while a high buffering capacity can diminish the pH inhibition at anode surface (Figure 3A and Figure S7). Our model indicated a strong decline of cell activity at the electrode surface by approximately 43%, but relatively less impact on overall current density (Figure 3B) when lowering bicarbonate buffer from 100 mM to 15 mM. This result is qualitatively consistent with the observation that lowering the phosphate buffer from 100 mM to 12.5 mM resulted in a > 80% decrease in the current production for an anode-respiring bacterial community, owing to the reduced H^+ transport capacity.[53] As a consequence, anode-respiring *G. sulfurreducens* biofilms may have an active outer-layer and an inactive inner layer if a low pH region develops within the inner layer due to poor buffering capacity of the media.

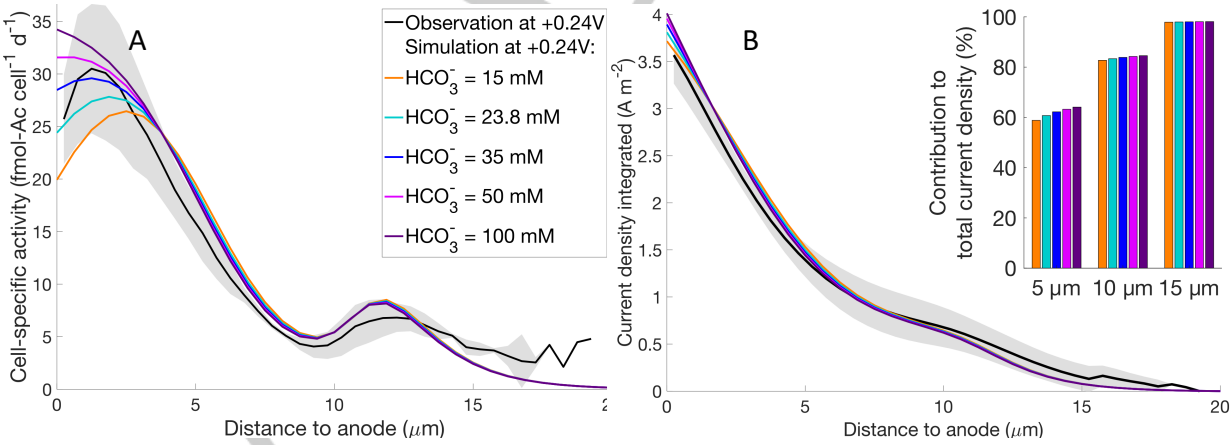

Figure 3. (A) The impact of bicarbonate buffering capacity on activity patterns at high anode potential for the activity peak near the electrode. (B) shows current density integrated over biofilm thickness and the fractional contribution at every 5 μm (inset). The shaded area represents 95% confidence interval for the observations

Electron conduction and storage within the *G. sulfurreducens* biofilms

Cell-specific electron transfer rate (e^- cell^{-1} s^{-1}) and current (fA cell^{-1}) were estimated using the modeled activity data shown in Figure 1. Model simulation results show maximum cell specific currents of approximately 200-250 fA cell^{-1} (1.25×10^6-1.5×10^6 e^- cell^{-1} s^{-1}) and 130 fA cell^{-1} (0.8×10^6 e^- cell^{-1} s^{-1}) near the electrode at high and low anode potential, respectively (Figure S8A), which is on the same order of magnitude as earlier reports on *G. sulfurreducens* DL-1 (~100 fA cell^{-1})[67], *Shewanella*

oneidensis MR-1 (75-200 fA cell^{-1})[68], and *S. loihica* PV-4 (100-400 fA cell^{-1})[69]. Furthermore, the simulated current densities (3.8 A m^{-2} and 1.3 A m^{-2} at high and low anode potential, respectively) compare favorably to those observed in the experiments modeled here (3-4 A m^{-2}) [58] and fall within the range of several reported microbial fuel cells using *G. sulfurreducens*[12, 70].

Our model simulations show redox potentials comparable to observations[59] (see Figure S8C). The redox gradient was the dominant driving force for electron transport in the system with low anode potential (Figure S8C), with a linear increase of Cyt_{ox} concentrations from about 10% of the [Cyt_{tot}] at the anode surface to approximately 70% at the outer edge of the biofilm at low anode potential (Figure S8D). This redox gradient leads to the reduction of redox-active centers coupled to acetate oxidation (Rxn 1) by *G. sulfurreducens* cells and the oxidation of redox-active centers at anode surface (Eq 13). The electric field (i.e. the voltage gradient) can also act as driving force for electron hopping, both when the electro-inactive counterions are immobilized[71-73] and mobile[74-76]. Our model suggests that electric field can be, but not necessarily is, an important additional driving force for electron transport towards the electrode (Figure S9A). Without the electric field as additional driving force, the cell specific activity pattern remains unaffected with an effective diffusion coefficient $D_{cyt} > 10^{-10}$ m^2 s^{-1} (Figure S9A&C), comparable to diffusion coefficients in dilute aqueous solution. At slower diffusion, the cell specific activity was significantly impacted due to the limited transport of Cyt_{red} (Figure S9B).

These model results are supported by observations on the distribution of reduced cytochromes, measurements of redox potential and electron storage: The modeled linear increase Cyt_{red} from the anode towards the bulk solution is consistent with the observed distribution of Cyt_{red} in *G. sulfurreducens* biofilms.[40-42, 77, 78] The increasing Cyt_{red} concentration towards the bulk-biofilm interface inevitably leads to a decreasing redox potential $\phi_{Ox/Red}$ ($\phi_{Ox/Red} = \phi^{0'}_{Ox/Red} + \frac{R_{gas}T}{F}\ln\left(\frac{[Cyt_{ox}]}{[Cyt_{red}]}\right)$ farther away from the anode surface (Figure S8D). Indeed, an earlier study directly observed that redox potential decreases significantly with increasing distance from the anode surface[59]. In addition, earlier redox titration studies showed that *G. sulfurreducens* biofilms or cytochromes were predominantly reduced at lower potentials,[39, 43, 79] agreeing with our simulation result overall (Figure S8E). However, those studies suggest that cytochrome would be substantially oxidized above +0.1V. The difference between the experimental observations and our simulations are likely attributed to the experimental procedure in which the cytochrome sample was purified[80, 81] or that *G. sulfurreducens* cells were starved and no acetate was provided prior and during the electrochemical titration[39, 43]. Finally, electron stored in reduced Cyt_{red} can be recovered as current when the electric potential is sufficient to transport electrons toward electrode.[41, 82] Assuming each Cyt_{red} holds one electron, under our modeled conditions the stored electrons in Cyt_{red} at steady state are estimated to be ~1.84-1.99×10^{-18} mol e$^-$ cell^{-1} and 0.8-3.4×10^{-18} mol e$^-$ cell^{-1} at high and low anode potential setting respectively, with more stored electrons in Cyt_{red} at the biofilm surface. Assuming minimum maintenance requirement at 1.9×10^{-2} mol e$^-$ gdw^{-1} h^{-1} [83] and biomass density ρ at 9.5×10^{-14} gdw cell^{-1} (Table 1), then the stored electrons in Cyt_{red} at steady state would be sufficient to support such a basic rate for approximately 7 min and 11 min at high and low anode potential setting, respectively, even when electrode is disconnected. This is similar to reported value (8 min) from Esteve-Núñez et al. (2008)[84].

Sensitivity analysis

Ten model parameters that are poorly constrained were considered in a sensitivity analysis. This included the critical switching potential (ϕ_c), the cell-specific rate constant (k_{cell}), the activation constant (k_{act}), the electron transport rate constant (k_D), the electric field driven rate constant (k_{EF}), the electrode discharge constant (k_{anode}), the abundance of redox-active molecules ([Cyt_{tot}]), the density of conductive network connections ($N_{nw,cell}$), biofilm conductivity (σ), and the redox-active cell surface area (A_{act}). To further explore the effect on the metabolic activity profiles, we varied the critical switching potential ϕ_c from -0.15 V to +0.05 V (Figure S2). As expected, increasing ϕ_c shifted the second activity peak towards the anode surface because ϕ_{net} crosses the critical threshold more rapidly (Figure S3). Eventually only one activity peak remained at critical potentials of -0.05 V and above, when $\phi_{net} < \phi_c$ even at the anode surface. Furthermore, the critical potential can increase the pH dependency, which exerts its effect primarily at the anode surface (Figure S4, and discussed below). It is noted that lowering biofilm resistance by increasing conductivity (σ) would shift the secondary metabolic peak further away from the electrode for the same ϕ_c (Fig. 4H and Fig. S12A, for ϕ_c = -0.15 V). Simply manipulating the value of ϕ_c does not lead to activity patterns consistent with observational data. This is due to the fact that lowering biofilm resistance also increases cell activity, as a result of reduced potential loss (Fig. S12C) and increased usable electric potential (ϕ_{net}) (Fig. S12B). In addition, pH also further decreases near the electrode as a result of increased cell activity (Fig. S12D).

Our results show that k_{cell} influenced the magnitude and location of both first and second metabolic peak, while k_{act} primarily influenced the location of first and second metabolic peak, k_{anode} mainly affected the magnitude of both first and second metabolic peak, k_D and k_{EF} showed negligible impact (Figure 4A-E). Although the relative magnitude of impact on potential losses and pH was limited (Figure S10), a reduction in k_{cell} and k_{anode} led to lower metabolic rates and diminished the first metabolic peak (Figure 4A&E) as a result of slightly increased pH (Figure S10D). Noticeably, the model results became less sensitive to k_{anode} at high values. For instance, increasing k_{anode} from 2.8×10^{-8} m s^{-1} to 1.12×10^{-7} m s^{-1} had little impact on the metabolic pattern (Figure 4E). It is noted that k_{anode} at 10^{-8} m s^{-1} corresponds to a electrode interfacial discharge rate constant k_{int} at ~14 s^{-1}. This is closely in agreement with the value (k_{int}= 13 ± 1 s^{-1}) reported from Bonanni et al. (2012)[82] and with other reported values [85, 86] as well for the typical heterogeneous oxidation rate of cytochromes at electrodes. This k_{int} at ~10 s^{-1} indicates a very fast and reversible kinetic process for the interfacial ET at the electrode[82].

In contrast, electrochemical properties of the *G. sulfurreducens* biofilm had a substantially greater impact on the metabolic activity (Figure 4F-H). Simulations show that [Cyt_{tot}] significantly influenced the magnitude and location of both first and second metabolic peak, while $N_{nw,cell}$, σ, and A_{act} primarily influenced the location of first and second metabolic peak. Increasing [Cyt_{tot}], $N_{nw,cell}$, σ and A_{act} increased the metabolic activity (Figure 4F-H), but also decreased the activity near the electrode by substantially lowering pH (Figure S10D). The abundance of redox-active molecules ([Cyt_{tot}]) and the density of conductive network connections ($N_{nw,cell}$) together represent the capacity of

extracellular electron transport network. In fact, $N_{nw,cell}$ is directly related to [Cyt_{tot}], with $N_{nw,cell} = [Cyt_{tot}]V_{bio}k_{nw}/N_{geo}$, where V_{bio} is the volume of biofilm dependent on biofilm thickness (L_{bio}) and electrode surface area (A_{anode}), and k_{nw} is the converting factor associated with conductive biofilm, and N_{geo} is the total number of *G. sulfurreducens* cells.

The effect of increasing or decreasing $N_{nw,cell}$ on the ohmic resistance can be counterbalanced by decreasing or increasing conductivity (σ), as evident from Eq. 11. Moreover, our model simulations showed that increasing biofilm conductivity four-fold to 0.06 S m^{-1} diminished the ohmic resistance loss (Figure S10A) in the *G. sulfurreducens* biofilms, while activation loss (Figure S10B) substantially increased and pH was significantly lowered (Figure S11D) near the electrode, thus making the electric potential more positive (Figure S10C). This is in line with an earlier study showing that biofilms with a relatively high conductivity (≥ 0.05 S m^{-1} [50] or ~ 0.1 S m^{-1} [51]) had negligible potential losses, with only proton transport being a limiting factor.[50]

Close examination of the anodic current density suggests that increasing those model parameters aforementioned, except the electron conduction rate constant (k_D) and electric field transport constant (k_{EF}), lead to an increase of current density at the anode (Figure 4). Earlier studies found that current density of *G. sulfurreducens* is correlated with biomass density (cells per unit anode surface area) on the anode[60]. Under conditions were growth efficiency remains relatively constant (see Figs. S1&S4), higher cell-specific activity implies higher biomass density assuming constant biofilm thickness. Four-fold changes in the abundance of redox-active molecules ([Cyt_{tot}]), the density of conductive network connections ($N_{nw,cell}$), biofilm conductivity (σ) led to an increase of current density by 43%, 29% and 25%, respectively, showing the importance of the electrochemical properties of the *G. sulfurreducens* biofilms for metabolic rates (Figure 4). Our simulation results suggest anodic current density can be increased even though the cell metabolism at the anode surface is limited by the accumulation of protons (Figure 4 and Figure S11).

Analyzing model parameter sensitivities also allowed us to assess the controversy over the stratification of cell activity in *G. sulfurreducens* biofilms, with reports of peak activities near[70, 78, 87-89] and away from the anode surface[61, 90]. Anode-respiring *G. sulfurreducens* biofilms may show a stratified biofilm structure with a live outer-layer and dead inner layer if a low pH region develops within the inner layer. As indicated by the metabolic activity profiles in Figure 4, the location of the peak cell-specific activity depends on the distinct electrochemical properties of the biofilm, which in turn affects current densities (Figure 4). It is possible that these electrochemical properties and metabolic activity can be regulated and optimized under different environment conditions.[91-95] As a consequence, different incubation conditions can lead to biofilms that have different abilities to control potential losses and H^+ transport yielding observations that differ in active cell layer stratification in *G. sulfurreducens* biofilms. [61, 70, 78, 87-90].

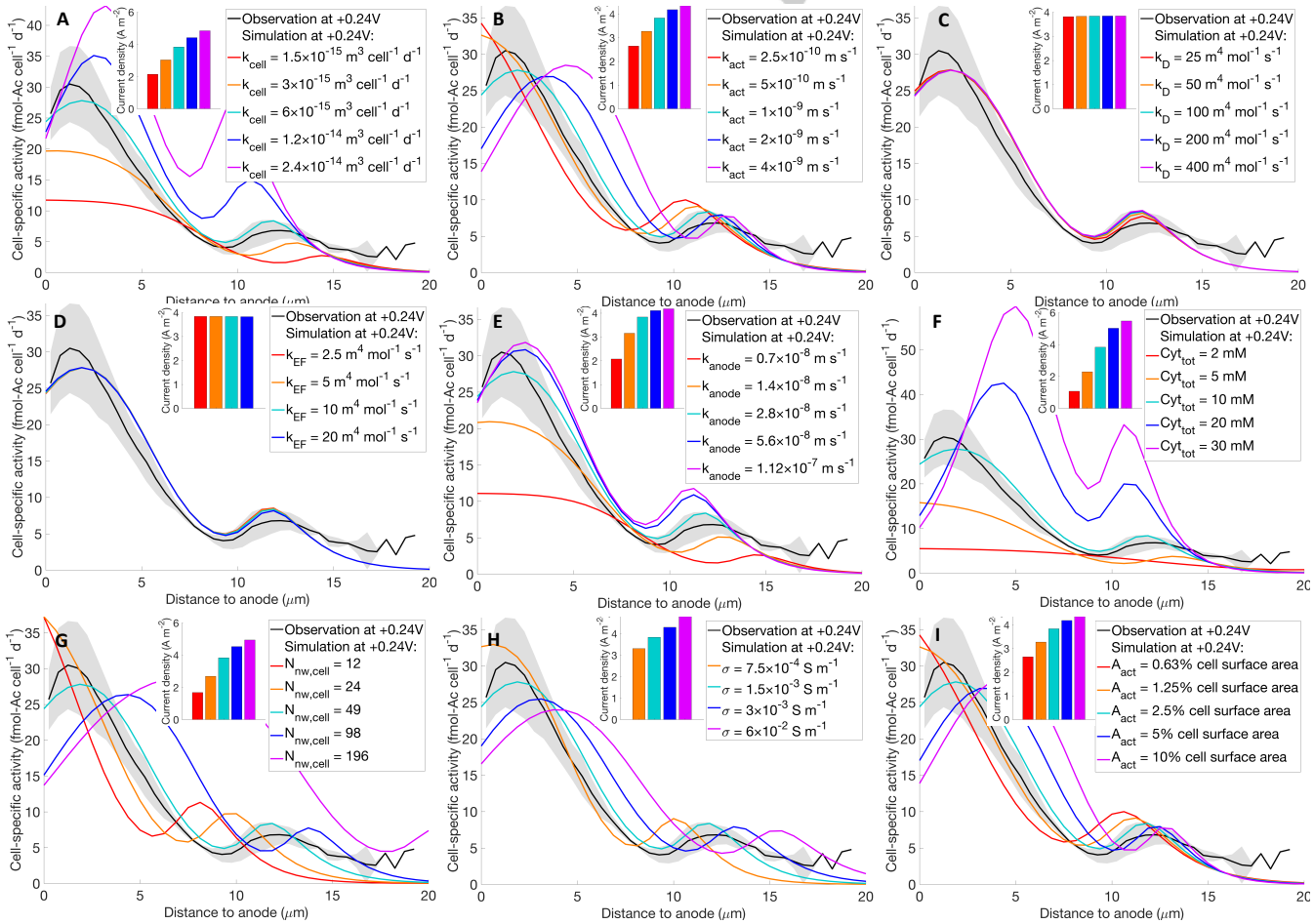

Figure 4. Sensitivity analysis of model parameters and their impact on cell specific activity and current density (inset): (A) cell-specific rate constant; (B) activation constant; (C) electron transport rate constant; (D) electric field driven rate constant; (E) electrode discharge constant; (F) the abundance of redox-active molecules; (G) the density of conductive network connections; (H) conductive biofilm conductivity; (I) redox-active cell surface area. Shaded area represents 95% confidence interval for observations.

Conclusion

Here we report on a model representation of a *G. sulfurreducens* biofilm that is able to reproduce high-resolution activity measurements of biofilms grown under more positive (+0.24 V) and more negative (-0.1 V) anode potentials.[58] Three major features of the metabolic activity patterns in the experimental data are captured in our model: 1) the maximum activity occurs near the anode surface in both high and low potential simulations, 2) at high potential a second activity peak occurs ~10 μm from electrode surface, and 3) a slight decrease in metabolic activity occurs right at the surface of the high potential anode. Central to these model results are potential losses and the accumulation of protons that in concert regulate the observed metabolic stratifications. Potential losses cause cells to experience lower effective potential than the value at which the anode is poised. These effects become more significant the further cells are from the anode surface causing the maximum metabolic activity to occur near the anode in both high and low potential simulations. Shifting between two redox-active systems allows *G. sulfurreducens* cells to respond to the decreasing external electric potential, leading to the secondary metabolic peak at ~12 μm from the electrode. No such secondary peak appears when the anode is poised at low potential because under these conditions the low potential redox-active system is the only one operative throughout the entire biofilm. At high anode potential our model reveals that H^+ accumulation close to the electrode limited *G. sulfurreducens* metabolism, leading to a slight decrease in metabolic activity at the electrode surface. This effect is not observed at low anodic potentials because the pH does not fall to values low enough to inhibit metabolic activity. Our model simulations also demonstrate how the redox gradients and electric fields that developed within *G. sulfurreducens* biofilms drive extracellular electron transfer through the biofilms to the electrode.

This model synthesizes existing knowledge and establishes a quantitative framework of the extracellular electron transfer in anode-respiring *G. sulfurreducens* biofilms that can further guide experimental studies on kinetic and electrochemical properties of *G. sulfurreducens* biofilms under different growth conditions. We have identified experimentally tunable parameters such as media buffering capacity that can lead to markedly different metabolic activity patterns, which can serve as valuable future experimental tests of the validity our modeling framework. Additionally, biofilms grown with mutant strains of *G. sulfurreducens* lacking the low potential redox-active system CbcL could test our prediction that the second activity peak is due to a switch in redox centers[64], providing a connection between genetically encoded metabolic proteins and cellular activity in biofilms. This approach of combining spatially resolved metabolic modeling with high resolution quantitative activity imaging provides much greater ability to constrain models, as compared to those only considering bulk processes such as the concentration of chemical species in the media and total current density.

Experimental Section

Experimental data

The experimental data used in this study are described in Chadwick et al. (2019). In brief, the anabolic activity of *G. sulfurreducens* biofilms was measured by ^{15}N fractional abundance using nanoSIMS.[58] *G. sulfurreducens* biofilms were incubated with $^{15}NH_4^+$ as the nitrogen in an anaerobic chamber with graphite electrodes (3 cm^2) serving as the electron acceptor. The electrode was poised at anode electric potentials of -0.1 V or +0.24 V vs. standard hydrogen electrode. Acetate (20 mM) was provided as the electron donor. After incubation for 6h (the duration of one doubling time), the intact *G. sulfurreducens* biofilms on the electrode were chemically fixed, embedded in resin, and thin sectioned. While these biofilms may be young compared to how long some set-ups are run, this was chosen specifically to try to understand what limits the exponential increase in current density during biofilm development. The timeframe captured in those experiments, and in our models, covers the major transition in biofilm current density increase from exponential to stationary phase. When exactly this transition occurs will vary based on reactor design or bacterial strain, but for any set-up there is always some maximum density that is reached. By modeling these experimental results we are able to comment on the factors that cause this cessation in exponential current density increase, which is one of the most important questions for engineering these systems. The most important feature of these experiments and results is the how the metabolic activity declines over increasing spatial distance from anode surface. To that end, our model is translatable to mature or mixed culture biofilms, as long as the fundamental mechanisms remain valid. Spatial patterns of anabolic activity (cellular ^{15}N incorporation) in the electrode-attached biofilm were then measured on a CAMECA nanoSIMS 50L instrument. Using cellular ^{15}N enrichment data, the growth rate (μ in d^{-1}) of *G. sulfurreducens* was calculated as

$$\mu = \frac{-\ln\left(1-\frac{F_{final}-F_{nat}}{F_{label}-F_{nat}}\right)}{T_{incub}} \quad \text{Eq (1)}$$

where T_{incub} is the length of the incubation (d), F_{label} is the labeling strength of the nitrogen source provided ($^{15}NH_4/(^{14}NH_4+^{15}NH_4)$ = 0.06), F_{final} is the ^{15}N fractional abundance measured in the biofilm using nanoSIMS, and F_{nat} = 0.0036 is the natural ^{15}N fractional abundance. The observed N assimilation is related to modeled metabolic rates through the growth yield (Y_{Ac} in grams dry weight per mol Ac oxidized), and cell-specific metabolic rates (R_{obs} in fmol-Ac $cell^{-1}$ d^{-1}) were calculated as

$$R_{obs} = \mu \cdot \frac{\rho}{Y_{Ac}} \quad \text{Eq (2)}$$

where ρ is biomass density (Table 1). Following King et al. (2009),[96] Y_{Ac} was calculated as a function of acetate uptake (U_{Ac}, see Eq 4)

$$Y_{Ac} = \max\left(0, a\frac{U_{Ac}-c}{b+U}\right) \quad \text{Eq (3)}$$

where the constants a, b and c are set to 5 grams dry weight (gdw) mol-Ac^{-1}, 2 mM-Ac gdw^{-1} h^{-1}, and 1 mM-Ac gdw^{-1} h^{-1}, respectively (Figure S1B). For the experimental conditions, this resulted in a growth yield Y_{Ac} of 4.32 gdw mol-Ac^{-1}, consistent with values reported in earlier experimental studies (ranging from 1 to 11 gdw mol-Ac^{-1}).[83, 97]

Model Description

The model describes acetate oxidation, with the produced electrons being transported to the anode via electron conduction. The rate of acetate oxidation is set to depend on both the acetate concentration, the availability of the extracellular electron acceptor, pH and the redox potential in the biofilm.

Metabolic Reactions

We model the EET in *G. sulfurreducens* biofilms with by representing three central processes: acetate uptake and oxidation with electron transfer to reduced redox-active molecules $Cyt_{red(Fe2+)}$, electron transport in conductive biofilm, and finally electron off-loading onto the anode.

Acetate uptake

The uptake of acetate (U_{Ac} in mM-Ac gdw^{-1} h^{-1}) can be described as a function of acetate availability[96] using

$$U_{Ac} = v_{max}\frac{[Ac]}{K_{m,Ac}+[Ac]} \quad \text{Eq (4)}$$

where v_{max} and $K_{m,Ac}$ are set to 20 mM-Ac gdw^{-1} h^{-1} and 10 μM, respectively, reflecting the relationships established in King et al. 2009 (Figure S1A).

Electron transfer to Cyt_{red} by acetate oxidation

Eight electrons are produced per mol Ac oxidized, in which a fraction (f_c) goes to catabolic reactions that produce CO_2, and the remainder is used in anabolic reactions (f_a, with $f_a + f_c = 1$) that produce biomass, which is represented by $CH_{1.8}O_{0.5}N_{0.2}$.[66] With that, the fraction of carbon that goes to biomass synthesis (f_a) from acetate oxidation is

$$f_a = \frac{Y_{Ac}}{24.6\,[g\ mol^{-1}]\times 2} \quad \text{Eq (5)}$$

where the factor of 2 represents 2 mol carbon goes to biomass ($CH_{1.8}O_{0.5}N_{0.2}$) per mol acetate oxidized.

The electron transfer from acetate oxidation to reduced redox-active molecules $Cyt_{red(Fe2+)}$ and CO_2 is given as

$$CH_3COO^- + f_a\frac{0.2}{0.525}NH_4^+ + \left(4f_c - f_a\frac{0.4}{0.525}\right)H_2O + 8f_cCyt_{ox(Fe^{3+})} \rightarrow \left(2f_c + f_a\frac{0.05}{0.525}\right)HCO_3^- + \frac{f_a}{0.525}CH_{1.8}O_{0.5}N_{0.2} + \left(9f_c - f_a\frac{0.275}{0.525}\right)H^+ + 8f_cCyt_{red(Fe^{2+})} \quad \text{Rxn (1)}$$

For convenience, we refer to $Cyt_{ox(Fe3+)}$ and $Cyt_{red(Fe2+)}$ as Cyt_{ox} and Cyt_{red}, respectively. We estimate the metabolic rate R_{geo} as a function of the availability of acetate and oxidized redox molecule Cyt_{ox}, as well as external constraints including an electric potential dependency (F_e) and a pH dependency (F_{pH}):

$$R_{geo} = k_{cell}B_{geo}\frac{[Ac]}{K_{m,Ac}+[Ac]}[Cyt_{ox}]\cdot F_\theta \cdot F_{pH} \quad \text{Eq (6)}$$

where k_{cell} is the cell-specific rate constant, B_{geo} is the cell density, $K_{m,Ac}$ is the half-saturation constant for acetate. The electric potential dependency (F_e) is formulated as a function of the electric potential in the biofilm, ϕ_{net} (see Eq 10),[49, 50, 98] leading to[50]

$$F_\theta = \frac{1}{e^{\frac{-F\left(\phi_{net}-\phi^{0'}_{\frac{Ox}{Red}}\right)}{RT}}+1} \quad \text{Eq (7)}$$

where $\phi^{0'}_{\frac{Ox}{Red}}$ is the mid-potential of the redox-active center. The pH dependency (F_{pH}) is expressed as

$$F_{pH} = \frac{2}{2+e^{-g(pH-C_{pH})}} \quad \text{Eq (8)}$$

where g = 20 and C_{pH} is varied in the simulation with a default value of 6.15. Eq (8) represents the pH impact on cell metabolism of *G. sulfurreducens*, which grow optimally at near-neutral pH[58]. Torres et al. (2009) showed that anode-respiring bacteria could be completely inhibited at pH values less than 6,[53] agreeing with the 99% decrease of metabolic rate at pH 5.9 reflected in Eq (8). This observation is further corroborated by findings of Franks et al. (2009) that indicate severe inhibition of *G. sulfurreducens* growth and 50% drop in current production by changing bulk pH from 6.9 to 6.15, and is consistent with the observed decrease in growth of *G. sulfurreducens* from 0.21 ± 0.1 h^{-1} to nearly zero (0.04 ± 0.02 h^{-1}) on the soluble electron acceptor fumarate when the pH decreased from 7 to 6.[54] See supplemental A11 for further discussion.

Electron conduction in G. sulfurreducens biofilms

Early studies indicated metallic-like conductive EET in *G. sulfurreducens*[12, 18, 99-101], where electrons are delocalized along a chain of molecules and are free to move throughout the material.[102] In contrast, electron hopping allows the electron transport between localized sites on a network of redox-active molecules (e.g. hemes) via tunneling or overcoming potential barriers, [14, 34, 41, 103-105] similar to electron conduction in other known organic molecules.[102, 106] This mechanism, which is explored here, is supported by experimental findings that reveal small spatial distances (a few Å) between those subunits[31] and the presence of heme redox gradient[41]. The electron hopping process in the presence of redox gradients (here the concentration gradient of Cyt_{red}) is commonly modeled as analogous to a random walk (second term on the right-hand side of Eq (9)), and the observed exponential dependence of the current on the electric potential gradient[71, 73] is represented by last term in Eq (9). Thus, electron conduction via electron hopping driven by redox gradient and electric field[73, 107] results in:

$$\frac{\partial[Cyt_{red}]}{\partial t} = 8f_cR_{geo} + \nabla\cdot\left(\boldsymbol{\mathcal{D}_{cyt}}\nabla[Cyt_{red}]\right) + \nabla\cdot\left(k_{EF}[Cyt_{ox}][Cyt_{red}]\left(\exp\left(\frac{\beta F\delta E}{R_{gas}T}\right) - \exp\left(-\frac{(1-\beta)F\delta E}{R_{gas}T}\right)\right)\right) \quad \text{Eq (9)}$$

where the first term on the right-hand side represents the loading of electrons onto Cyt_{ox} at the location of acetate oxidation. $D_{cyt} = k_D[Cyt_{tot}]\delta$ is an effective diffusion coefficient, k_D is the electron transfer rate constant, [Cyt_{tot}] is the total concentration (= [Cyt_{ox}] + [Cyt_{red}]), δ is the spatial distance between adjacent redox-active molecules, E is the local electric field, and β is the charge transfer coefficient (see Table 1). The electric potential in the biofilm (ϕ_{net}) is described by

$$\phi_{net} = \phi_{anode} - \phi_{om} - \phi_{act} \quad \text{Eq (10)}$$

where ϕ_{anode} is the poised anode potential, ϕ_{om} and ϕ_{act} are the ohmic and activation voltage losses, respectively. ϕ_{om} is expressed as [108]

$$\phi_{om} = \frac{R_{nw}I}{N_{nw}} = \frac{d}{\sigma A_{nw}}\frac{8f_cR_{geo}N_{geo}F}{Cyt_{tot}V_{bio}k_{nw}} \quad \text{Eq (11)}$$

where I is the current produced by acetate oxidation ($I = 8f_cR_{geo}N_{geo}F$), N_{geo} is the number of *G. sulfurreducens* cells, R_{nw} is the electrical resistance (Ω) which can be further described as $d/(\sigma A_{nw})$, σ is the biofilm conductivity, d is the distance from the anode surface, A_{nw} is the cross-section area of a single connecting filament, N_{nw} is the total conductive connections and can be described as a function of total redox-active molecule concentration [Cyt_{tot}], the volume of *G. sulfurreducens* biofilm V_{bio} by directly applying $N_{nw} = [Cyt_{tot}]V_{bio}k_{nw}$, where k_{nw} is the converting factor associated with conductive biofilm. ϕ_{act} is described using Butler-Volmer equation by[108]

$$I = N_{nw}FA_{act}k_{act}[Cyt_{tot}]\left(\exp\left(\frac{(1-\beta)F}{R_{gas}T}\phi_{act}\right) - \exp\left(\frac{-\beta F}{R_{gas}T}\phi_{act}\right)\right) \quad \text{Eq (12)}$$

where A_{act} is the redox molecule surface area per cell in m^2 and k_{act} is the redox molecule electron transport rate constant (m s^{-1}). Note that the modeled ohmic loss and activation loss depend on the value of $N_{nw}\sigma$ and $N_{nw}A_{act}k_{act}$, respectively, where N_{nw} is the product of cell-specific connection numbers ($N_{nw,cell}$) and the cell density (N_{geo}). Although the number of conductive filaments in the *G.*

sulfurreducens biofilms was not quantified in the experiments modeled here, TEM images of the conductive network produced by *G. sulfurreducens* [32, 109-111] suggest numerous conductive connections per cell. We set the number of conductive network connections $N_{nw,cell}$ to 49 in our base model, in the range considered by Storck et al. (2016)[108], and explored a wider range.

At the anode, electrons are transferred from Cyt_{red} to the electrode:

$Cyt_{red}|_{anode} \rightarrow Cyt_{ox}|_{anode} + e^-|_{anode \rightarrow cathode}$ Rxn (2)

The flux of electrons to the anode can be described using the Butler–Volmer equation [82]

$$J_c = k_{anode}\left([Cyt_{red}]\exp\left(\frac{\beta F}{R_{gas}T}\left(\phi_{anode} - \phi^{0'}_{\frac{Ox}{Red}}\right)\right) - [Cyt_{ox}]\exp\left(\frac{-(1-\beta)F}{R_{gas}T}\left(\phi_{anode} - \phi^{0'}_{\frac{Ox}{Red}}\right)\right)\right) \quad \text{Eq (13)}$$

where $k_{anode} = k_{int} \times \delta$, is electron off-loading constant that varies with the imposed electrode potential, and k_{int} is the rate constant of the discharge at the electrode [82]. The difference in k_{anode} at more postive (+0.24V) and more negative potential (-0.1V) reflects the observation that when biofilms grown at low potential were switched to high potential for the short duration of the isotope labeling experiment, the activity pattern appeared to retain that of a low potential biofilm, suggesting that some features of the biofilm matrix or cell metabolic systems were different between the two conditions (Figure 5F in reference [58]). Notably, the value of k_{anode} did not affect the shape of the metabolic profile in the low potential simulations, but was necessary to match the maximum observed in the cell activity in the experimental data.

Shift of redox pair mid-potential as a function of external potential

Experimental studies have shown that redox-active molecule mid-potential in *G. sulfurreducens* outer membrane can be regulated by the anode electric potential, [45, 46] and are also observed in *G. sulfurreducens* biofilms[43, 44, 112, 113] or mixed bioanode community [56] with at least two different types of redox-active molecule pairs with mid-potentials near -0.07 V and -0.15 V, respectively. It has been noted that the low mid-potential redox centers (-0.15 V) are required for cells to function under low electrode potential, while the redox centers poised at -0.07 V only operate at high electrode potential.[45, 46] In our model, this is represented by a switch function that shifts the mid-potential from -0.07 V to -0.15 V at a critical potential ϕ_c. In order to mimic the response of the change of external potential we implement the redox pair mid-potential as a continuous function (see Figure S2):

$$\phi^{0'}_{\frac{Ox}{Red}} = \frac{x}{e^{y(\phi_{net}-\phi_c)}+1} + z \quad \text{Eq (14)}$$

where constants x, y, and z are set to 0.08 V, -90 [1/V], and -0.15 V, respectively. ϕ_c is the critical shifting potential for mid-potential of redox-active center with a default value of -0.15 V.

Model implementation

Reflecting the observations of Chadwick et al. (2019), which showed that the variation in ^{15}N uptake is predominantly in the direction perpendicular to the electrode surface, a one-dimensional dynamic model was implemented in COMSOL Multiphysics 5.4 (COMSOL Inc., Burlington, MA, USA). Batch simulations exploring the parameter space were executed using MATLAB 2018 (MathWorks, Natick, MA, USA), and simulations were run to steady state. Matching the observational data, the thickness of the biofilm was set to 20 μm and 15 μm for simulations under high (+0.24 V) and low (-0.1 V) anode potentials, respectively, with a 1.8 mm bulk-liquid environment beyond the biofilm surface. The concentration fields of acetate, HCO_3^-, CO_2(aq), CO_3^{2-}, H^+, and OH^- were simulated subject to diffusive transport and reaction, with aqueous diffusion coefficients listed in Table 1. Acid-base reactions govern the dynamic carbonate system and the speciation of cell surface-associated immobile carboxy (R-COOH), phosphate ($R\text{-}PO_4H_2$) and amino groups ($R\text{-}NH_2$) are simulated using the kinetic implementation described previously [114]. The concentrations at the outer domain boundary were set to fixed concentrations reflecting environmental conditions (Table 1 and S1), which were also used as initial conditions. No flux conditions were imposed at the anode surface, where Cyt_{red} was converted to Cyt_{ox} at a rate set by J_c, representing the off-loading of electrons to electrode.

Table 1. Key model parameter and description

Symbol	Units	Value (baseline value)	Description	Reference
Cell growth and Kinetics				
k_{cell}	m^3 $cell^{-1}$ d^{-1}	10^{-14} -10^{-16} (6×10^{-15})	Cell-specific acetate consumption rate constant	Estimated from [6]
μ	d^{-1}	varied	Cell growth rate	Calculated using Eq (1)
ρ	gdw $cell^{-1}$	9.5×10^{-14}	Biomass density	Estimated from[115]
Y_{Ac}	gdw mol-Ac^{-1}	4.32	Growth yield	Calculated using Eq (3)
U_{Ac}	mM-Ac gdw^{-1} h^{-1}		Uptake of acetate	Calculated using Eq (4)
v_{max}	mM-Ac gdw^{-1} h^{-1}	20	Maximum uptake rate of acetate	[96]
$K_{m,Ac}$	μM	10	Half-saturation concentration of acetate	
Electron conduction				
Cyt_{tot}	mM	1-100 (10)	Total redox-active molecules ($Cyt_{tot} = Cyt_{ox} + Cyt_{red}$)	Estimated from[66, 116]

D_{cyt}	$m^2\ s^{-1}$	10^{-5}-10^{-10} (7×10^{-7})	Effective diffusion coefficient	Estimated from[116-118]
k_D	$m^4\ mol\ s^{-1}$	10^{-5}-10^{5} (100)	Electron transfer rate constant	Estimated from $D_{cyt} = k_D[Cyt_{tot}]\delta$
δ	nm	0.7	Spatial distance between adjacent redox-active molecules	[119]
σ	$S\ m^{-1}$	10^{-4}-10^{-2} (1.5×10^{-3})	Biofilm conductivity	[12, 21, 35, 120]
A_{nw}	m^2	1.26×10^{-17}	Cross-section area of a single pilus	Calculated from d_{nw}
d_{nw}	nm	4	Diameter of a single pilus	[31, 32]
A_{act}	m^2	10^{-14}-10^{-13}	Redox active surface area	Estimated from [108]
β	-	0.5	Charge transfer coefficient	[108]
ϕ_{anode}	V	-0.1, +0.24	Poised low, high anode potential	[58]
$\phi_{ox/red}^{0'}$	V	-0.07, -0.15	Redox-active center mid-potential	[44, 56]
$N_{nw,cell}$	-	1-200 (49)	Number of connections per cell	Estimated from [32, 108-111]

Fixed concentration were imposed for all chemical species at the outer domain boundary except for CO_2, CO_3^{2-}, Cyt_{red}, $R\text{-}COOH$, $R\text{-}NH_2$, $R\text{-}PO_4H_2$. No flux conditions were imposed at the bulk-biofilm interface and anode surface for CO_2, CO_3^{2-}, Cyt_{red}. Fixed concentration were imposed for all chemical species at the anode surface except for Cyt_{red}, for which a flux J_c to Cyt_{ox} (Eq. 13) was imposed to represent the electron discharge onto electrode. Boundary conditions are set to: 20 mM acetate, 23.8 mM HCO_3^-, pH = 6.8.

Acknowledgements

This work was supported by the U.S. Department of Energy, Office of Science, Office of Biological and Environmental Research, Genomic Science Program under Award Number DE-SC0016469 and DE-SC0020373 (to CM and VJO). Contributions by VJO and GC were also supported in part by a grant from the Simons Foundation (#542393) part of the Principles of Microbial Ecosystems Collaborative (PriME). We thank D. Bond for assisting with the initial G. sulfurreducens bioreactor experiments used in this study.

Keywords: Microbial fuel cells • *Geobacter sulfurreducens* • electroactive biofilms • direct extracellular electron transfer • nanoSIMS

[1] A.-E. Rotaru, P. M. Shrestha, F. Liu, B. Markovaite, S. Chen, K. P. Nevin, D. R. Lovley, *Appl. Environ. Microbiol.* **2014,** *80*, 4599-4605.
[2] N. S. Malvankar, M. Vargas, K. P. Nevin, A. E. Franks, C. Leang, B. C. Kim, K. Inoue, T. Mester, S. F. Covalla, J. P. Johnson, V. M. Rotello, *Nat. Nanotechnol.* **2011,** *6*, 573-579.
[3] B. Virdis, D. Millo, B. C. Donose, Y. Lu, D. J. Batstone, J. O. Krömer, *RSC Adv.* **2016,** *6*, 3650–3660.
[4] M. V. Ordóñez, G. D. Schrott, D. A. Massazza, J. P. Busalmen, *Energy Environ Sci* **2016,** *9*, 2677–2681.
[5] S. H. Saunders, E. C. M. Tse, M. D. Yates, F. J. Otero, S. A. Trammell, E. D. A. Stemp, J. K. Barton, L. M. Tender, D. K. Newman, *Cell* **2020,** *182*, 919-932.
[6] X. He, G. Chadwick, C. Kempes, Y. Shi, S. McGlynn, V. Orphan, C. Meile, *Environ. Microbiol.* **2019,** *21*, 631-647.
[7] Z. M. Summers, H. E. Fogarty, C. Leang, A. E. Franks, N. S. Malvankar, D. R. Lovley, *Science* **2010,** *330*, 1413–1415.
[8] M. P. Manzella, G. Reguera, K. Kashefi, *Appl. Environ. Microbiol.* **2013,** *79*, 4694-4700.
[9] F. Kracke, I. Vassilev, J. O. Krömer, *Front. Microbiol.* **2015,** *6*, 575.
[10] D. L. Cologgi, S. Lampa-Pastirk, A. M. Speers, S. D. Kelly, G. Reguera, *Proc. Natl. Acad. Sci. U. S. A.* **2011,** *108*, 15248–15252.
[11] D. R. Bond, D. R. Lovley, *Appl. Environ. Microbiol.* **2003,** *69*, 1548–1555.
[12] N. S. Malvankar, M. T. Tuominen, D. R. Lovley, *Energy Environ. Sci.* **2012,** *5*, 5790-5797.
[13] N. S. Malvankar, M. T. Tuominen, D. R. Lovley, *Energy Environ. Sci.* **2012,** *5*, 6247-6249.
[14] S. M. Strycharz-Glaven, R. M. Snider, A. Guiseppi-Elie, L. M. Tender, *Energy Environ. Sci.* **2011,** *4*, 4366–4379.
[15] S. M. Strycharz-Glaven, L. M. Tender, *Energy Environ. Sci.* **2012,** *5*, 6250-6255.
[16] M. D. Yates, S. M. Strycharz-Glaven, J. P. Golden, J. Roy, S. Tsoi, J. S. Erickson, M. Y. El-Naggar, S. C. Barton, L. M. Tender, *Nat. Nanatechnol.* **2016,** *11*, 910-913.
[17] N. S. Malvankar, V. M. Rotello, M. T. Tuominen, D. R. Lovley, *Nat. Nanatechnol.* **2016,** *11*, 913–914.
[18] N. S. Malvankar, M. Vargas, K. P. Nevin, A. E. Franks, C. Leang, B.-C. Kim, K. Inoue, T. Mester, S. F. Covalla, J. P. Johnson, V. M. Rotello, M. T. Tuominen, D. R. Lovley, *Nat. Nanatechnol.* **2011,** *6*, 573-579.
[19] S. E. Yalcin, N. S. Malvankar, *Curr. Opin. Chem. Biol.* **2020,** *59*, 193-201.
[20] IUPAC, 2nd ed.; Blackwell Scientific Publications: Oxford, 1997; Vol. ISBN 0-9678550-9-8. https://doi.org/10.1351/goldbook.
[21] R. Y. Adhikari, N. S. Malvankar, M. T. Tuominen, D. R. Lovley, *RSC Adv.* **2016,** *6*, 8354–8357.
[22] N. S. Malvankar, M. Vargas, K. P. Nevin, A. E. Franks, C. Leang, B.-C. Kim, K. Inoue, T. Mester, S. F. Covalla, J. P. Johnson, V. M. Rotello, M. T. Tuominen, D. R. Lovley, *Nat Nanotechnol* **2011,** *6*, 573–579.
[23] M. Vargas, N. S. Malvankar, P. L. Tremblay, C. Leang, J. A. Smith, P. Patel, O. Synoeyenbos-West, K. P. Nevin, D. R. Lovley, *mBio* **2013,** *4*, e00105-13.
[24] N. S. Malvankar, M. Vargas, K. Nevin, P. L. Tremblay, K. Evans-Lutterodt, D. Nykypanchuk, E. Martz, M. T. Tuominen, D. R. Lovley, *mBio* **2015,** *6*, e00084-15.
[25] D. N. Blauch, J. M. Saveant, *J. Am. Chem. Soc.* **1992,** *114*, 3323-3332.
[26] M. Cordes, A. Köttgen, C. Jasper, O. Jacques, H. Boudebous, B. Giese, *Angew. Chem., Int. Ed.* **2008,** *47*, 3461-3463.
[27] J. R. Winkler, H. B. Gray, *Chemical Reviews* **2014,** *114*, 3369-3380.
[28] S. Skourtis, I. A. Balabin, T. Kawatsu, D. N. Beratan, *Proc. Natl. Acad. Sci. U. S. A.* **2005,** *102*, 3552-3557.
[29] E. W. Schlag, S. Y. Sheu, D. Y. Yang, H. L. Selzle, S. H. Lin, *Angew. Chem., Int. Ed.* **2007,** *119*, 3258-3273.
[30] S. Pirbadian, M. Y. El-Naggar, *Phys. Chem. Chem. Phys.* **2012,** *14*, 13802-13808.

[31] F. Wang, Y. Gu, J. P. O'Brien, M. Y. Sophia, S. E. Yalcin, V. Srikanth, C. Shen, D. Vu, N. L. Ing, A. I. Hochbaum, E. H. Egelman, *Cell* **2019,** *177*, 361-369.
[32] D. J. Filman, S. F. Marino, J. E. Ward, L. Yang, Z. Mester, E. Bullitt, D. R. Lovley, M. Strauss, *Commun. Biol.* **2019,** *2*, 1-6.
[33] S. E. Yalcin, J. P. O'Brien, Y. Gu, K. Reiss, M. Y. Sophia, R. Jain, V. Srikanth, P. J. Dahl, W. Huynh, D. Vu, A. Acharya, *Nat. Chem. Biol.* **2020,** *16*, 1136-1142.
[34] D. R. Bond, S. M. Strycharz‐Glaven, L. M. Tender, C. I. Torres, *ChemSusChem* **2012,** *5*, 1099-1105.
[35] M. D. Yates, J. P. Golden, J. Roy, S. M. Strycharz-Glaven, S. Tsoi, J. S. Erickson, M. Y. El-Naggar, S. C. Barton, L. M. Tender, *Phys. Chem. Chem. Phys.* **2015,** *17*, 32564-32570.
[36] M. Yates, S. Strycharz-Glaven, J. Golden, J. Roy, S. Tsoi, J. Erickson, M. El-Naggar, S. C. Barton, L. Tender, *J. Visualized Exp.* **2018,** *136*, e54671.
[37] H. Phan, M. D. Yates, N. D. Kirchhofer, G. C. Bazan, L. M. Tender, T. Q. Nguyen, *Phys. Chem. Chem. Phys.* **2016,** *18*, 17815-17821.
[38] S. Lampa-Pastirk, J. P. Veazey, K. A. Walsh, G. T. Feliciano, R. J. Steidl, S. H. Tessmer, G. Reguera, *Sci. Rep.* **2016,** *6*, 23517.
[39] Y. Liu, H. Kim, R. R. Franklin, D. R. Bond, *ChemPhysChem* **2011,** *12*, 2235– 2241.
[40] Y. Liu, D. R. Bond, *ChemSusChem* **2012,** *5*, 1047–1053.
[41] N. Lebedev, S. M. Strycharz-Glaven, L. M. Tender, *ChemPhysChem* **2014,** *15*, 320– 327.
[42] R. M. Snider, S. M. Strycharz-Glaven, S. D. Tsoi, J. S. Erickson, L. M. Tender, *Proc. Natl. Acad. Sci. U. S. A.* **2012**, 15467–15472.
[43] D. B. Li, J. Li, D. F. Liu, X. Ma, L. Cheng, W. W. Li, C. Qian, Y. Mu, H. Q. Yu, *Biotechnol. Bioeng.* **2019,** *116*, 961-971.
[44] R. A. Yoho, S. C. Popat, C. I. Torres, *ChemSusChem* **2014,** *7*, 3413-3419.
[45] C. E. Levar, C. H. Chan, M. G. Mehta-kolte, D. R. Bond, *mBio* **2014,** *5*, 1-9.
[46] L. Zacharoff, C. H. Chan, D. R. Bond, *Bioelectrochemistry* **2016,** *107*, 7-13.
[47] C. Meile, T. D. Scheibe, *Elements* **2019,** *15*, 111-116.
[48] C. Picioreanu, M. C. van Loosdrecht, T. P. Curtis, K. Scott, *Bioelectrochemistry* **2010,** *78*, 8-24.
[49] A. K. Marcus, C. I. Torres, B. E. Rittmann, *Biotechnol. Bioeng.* **2007,** *98*, 1171-1182.
[50] C. I. Torres, A. K. Marcus, P. Parameswaran, B. E. Rittmann, *Environ. Sci. Technol.* **2008,** *42*, 6593-6597.
[51] C. I. Torres, A. K. Marcus, H. S. Lee, P. Parameswaran, R. Krajmalnik-Brown, B. E. Rittmann, *FEMS Microbiol. Rev.* **2010,** *34*, 3-17.
[52] B. Korth, F. Harnisch, *Front. Microbiol.* **2019,** *10*, 1352.
[53] C. Torres, A. Kato Marcus, B. Rittmann, *Biotechnol. Bioeng.* **2008,** *100*, 872-881.
[54] A. E. Franks, K. P. Nevin, H. F. Jia, M. Izallalen, T. L. Woodard, D. R. Lovley, *Energy Environ. Sci.* **2009,** *2*, 113–119.
[55] B. E. Logan, *Nat. Rev. Microbiol.* **2009,** *7*, 375-381.
[56] M. Rimboud, E. D.-L. Quemener, B. Erable, T. Bouchez, A. Bergel, *Bioresour. Technol.* **2015,** *195*, 192-169.
[57] R. A. Yoho, S. C. Popat, L. Rago, A. Guisasola, C. I. Torres, *Langmuir* **2015,** *31*, 12552-12559.
[58] G. L. Chadwick, F. J. Otero, J. A. Gralnick, D. R. Bond, V. J. Orphan, *Proc. Natl. Acad. Sci. U. S. A.* **2019,** *116*, 20716-20724.
[59] J. T. Babauta, H. D. Nguyen, T. D. Harrington, R. Renslow, H. Beyenal, *Biotechnol Bioeng.* **2012,** *109*, 2651–2662.
[60] S. I. Ishii, K. Watanabe, S. Yabuki, B. E. Logan, Y. Sekiguchi, *Appl. Environ. Microbiol.* **2008,** *74*, 7348-7355.
[61] D. Sun, J. Chen, H. Huang, W. Liu, Y. Ye, S. Cheng, *Int. J. Hydrogen Energy* **2016,** *41*, 16523-16528.
[62] P. S. Bonanni, D. F. Bradley, G. D. Schrott, J. P. Busalmen, *ChemSusChem* **2013,** *6*, 711-720.
[63] S. Larsson, *J. Supercond. Nov. Magn.* **2017,** *30*, 275-285.
[64] C. E. Levar, C. L. Hoffman, A. J. Dunshee, B. M. Toner, D. R. Bond, *ISME J.* **2017,** *11*, 741-752.
[65] C. I. Torres, A. K. Marcus, P. Parameswaran, B. E. Rittmann, *Environ. Sci. Technol.* **2008,** *42*, 6593–6597.
[66] B. Korth, L. F. Rosa, F. Harnisch, C. Picioreanu, *Bioelectrochemistry* **2015,** *106*, 194-206.
[67] X. Jiang, J. Hu, E. R. Petersen, L. A. Fitzgerald, C. S. Jackan, A. M. Lieber, B. R. Ringeisen, C. M. Lieber, J. C. Biffinger, *Nat. Commun.* **2013,** *4*, 1-6.
[68] J. S. McLean, G. Wanger, Y. A. Gorby, M. Wainstein, J. McQuaid, S. I. Ishii, O. Bretschger, H. Beyenal, K. H. Nealson, *Environ. Sci. Technol.* **2010,** *44*, 2721-2727.
[69] H. Liu, G. J. Newton, R. Nakamura, K. Hashimoto, S. Nakanishi, *Angew. Chem., Int. Ed.* **2010,** *49*, 6596-6599.
[70] K. P. Nevin, H. Richter, S. F. Covalla, J. P. Johnson, T. L. Woodard, A. L. Orloff, H. Jia, M. Zhang, D. R. Lovley, *Environ. Microbiol.* **2008,** *10*, 2505-2514.
[71] J. C. Jernigan, N. A. Surridge, M. E. Zvanut, M. Silver, R. W. Murray, *J. Phys. Chem.* **1989,** *93*, 4620-4627.
[72] J. C. Jernigan, R. W. Murray, *J. Phys. Chem.* **1987,** *91*, 2030-2032.
[73] E. F. Dalton, N. A. Surridge, J. C. Jernigan, K. O. Wilbourn, J. S. Facci, R. W. Murray, *Chem. Phys.* **1990,** *141*, 143-157.
[74] J. M. Savéant, *J. Electroanal. Chem.* **1988,** *242*, 1-21.
[75] J. M. Savéant, *J. Electroanal. Chem.* **1986,** *201*, 211-213.
[76] R. P. Buck, *J. Electroanal. Chem.* **1987,** *219*, 23-48.
[77] L. Robuschi, J. P. Tomba, G. D. Schrott, P. S. Bonanni, P. M. Desimone, J. P. Busalmen, *Angew. Chem., Int. Ed.* **2013,** *52*, 925-928.
[78] R. J. Steidl, S. Lampa-Pastirk, G. Reguera, *Nat. Commun.* **2016,** *7*, 12217.
[79] A. Jain, G. Gazzola, A. Panzera, M. Zanoni, E. Marsili, *Electrochim. Acta* **2011,** *56*, 10776–10785.
[80] K. Inoue, X. Qian, L. Morgado, B.-C. Kim, T. Mester, M. Izallalen, C. A. Salgueiro, D. R. Lovley, *Appl. Environ. Microbiol.* **2010,** *76*, 3999-4007.
[81] X. Qian, T. Mester, L. Morgado, T. Arakawa, M. L. Sharma, K. Inoue, C. Joseph, C. A. Salgueiro, M. J. Maroney, D. R. Lovley, *Biochim. Biophys. Acta* **2011,** *1807*, 404-412.
[82] P. S. Bonanni, G. D. Schrott, L. Robuschi, J. P. Busalmen, *Energy Environ. Sci.* **2012,** *5*, 6188-6195.
[83] A. Esteve-Núñez, M. Rothermich, M. Sharma, D. Lovley, *Environ. Microbiol.* **2005,** *7*, 641-648.
[84] A. Esteve‐Núñez, J. Sosnik, P. Visconti, D. R. Lovley, *Environ. Microbiol.* **2008,** *10*, 497-505.
[85] A. E. Nassar, J. Schenkman, J. Rusling, *J. Chem. Soc., Faraday Trans.* **1997,** *93*, 1769-1774.\.
[86] W. J. Albery, M. J. Eddowes, H. A. O. Hill, A. R. Hillman, *J. Am. Chem. Soc.* **1981,** *103*, 3904-3910.
[87] G. D. Schrott, M. V. Ordoñez, L. Robuschi, J. P. Busalmen, *ChemSusChem* **2014,** *7*, 598–603.
[88] G. Reguera, K. P. Nevin, J. S. Nicoll, S. F. Covalla, T. L. Woodard, D. R. Lovley., *Appl. Environ. Microbiol.* **2006,** *72*, 7345-7348.
[89] A. E. Franks, R. H. Glaven, D. R. Lovley, *ChemPhysChem* **2012,** *5*, 1092–1098.
[90] D. Sun, S. Cheng, F. Zhang, B. E. Logan, *J. Power Sources* **2017,** *356*, 566–571.
[91] L. V. Richter, S. J. Sandler, R. M. Weis, *J. Bacteriol.* **2012,** *194*, 2551-2563.
[92] T. Ueki, D. R. Lovley, *Nucleic Acids Res.* **2010,** *38*, 810–821.
[93] K. P. Nevin, B.-C. Kim, R. H. Glaven, J. P. Johnson, T. L. Woodard, B. A. Methé, R. J. DiDonato Jr, S. F. Covalla, A. E. Franks, A. Liu, D. R. Lovley, *PLoS ONE* **2008,** *4*, e5628.
[94] D. E. Holmes, S. K. Chaudhuri, K. P. Nevin, T. Mehta, B. A. Methé, A. Liu, J. E. Ward, T. L. Woodard, J. Webster, D. R. Lovley, *Environ. Microbiol.* **2006,** *8*, 1805-1815.
[95] Y. H. R. Ding, K. K. Hixson, C. S. Giometti, A. Stanley, A. Esteve-Núñez, T. Khare, S. L. Tollaksen, W. Zhu, J. N. Adkins, M. S. Lipton, R. D. Smith, *Biochim. Biophys. Acta* **2006,** *1764*, 1198-1206.
[96] E. L. King, K. Tuncay, P. Ortoleva, C. Meile, *Appl. Environ. Microbiol.* **2009,** *75*, 83-92.
[97] Y. J. Tang, R. Chakraborty, H. G. Martín, J. Chu, T. C. Hazen, J. D. Keasling, *Appl. Environ. Microbiol.* **2007,** *73*, 3859–3864.
[98] D. E. LaRowe, A. W. Dale, J. P. Amend, P. Van Cappellen, *Geochim. Cosmochim. Acta* **2012,** *90*, 96-109.
[99] N. S. Malvankar, S. E. Yalcin, M. T. Tuominen, D. R. Lovley, *Nat Nanotechnol* **2014,** *9*, 1012– 1017.
[100] N. S. Malvankar, T. Mester, M. T. Tuominen, D. R. Lovley, *ChemPhysChem* **2012,** *13*, 463–468.
[101] N. S. Malvankar, M. T. Tuominen, D. R. Lovley, *Energy Environ. Sci.* **2012,** *5*, 8651-8659.
[102] P. P. Edwards, H. B. Gray, M. T. J. Lodge, R. J. P. Williams, *Angew. Chem., Int. Ed.* **2008,** *47*, 6758–6765.
[103] S. M. Strycharz, A. P. Malanoski, R. M. Snider, H. Yi, D. R. Lovley, L. M. Tender, *Energy Environ. Sci* **2011,** *4*, 896-913.
[104] H. Yan, C. Chuang, A. Zhugayevych, S. Tretiak, F. W. Dahlquist, G. C. Bazan, *Adv. Mater.* **2015,** *27*, 1908-1911.
[105] P. S. Bonanni, D. Massazza, J. P. Busalmen, *Phys. Chem. Chem. Phys.* **2013,** *15*, 10300-10306.
[106] M. Waleed Shinwari, M. Jamal Deen, E. B. Starikov, G. Cuniberti, *Adv. Funct. Mater.* **2010,** *20*, 1865–1883.
[107] J. Saito, M. Murugan, X. Deng, A. Guionet, W. Miran, A. Okamoto, Electrochemical Techniques and Applications to Characterize Single- and Multicellular Electric Microbial Functions. In *Bioelectrochemical Interface Engineering*, Krishnaraj, R. N.; Sani, R. K., Eds. John Wiley & Sons, Inc.: Hoboken, NJ, 2020; pp 37-54.
[108] T. Storck, B. Virdis, D. J. Batstone, *ISME J* **2016,** *10*, 621-631.
[109] X. Liu, H. Gao, J. E. Ward, X. Liu, B. Yin, T. Fu, J. Chen, D. R. Lovley, J. Yao, *Nature* **2020,** *578*, 550-554.
[110] Y. Tan, R. Y. Adhikari, N. S. Malvankar, S. Pi, J. E. Ward, T. L. Woodard, K. P. Nevin, Q. Xia, M. T. Tuominen, D. R. Lovley, *Small* **2016,** *12*, 4481-4485.
[111] T. Fu, X. Liu, H. Gao, J. E. Ward, X. Liu, B. Yin, Z. Wang, Y. Zhuo, D. J. Walker, J. J. Yang, J. Chen, *Nat Commun* **2020,** *11*, 1-10.
[112] L. Peng, X. T. Zhang, J. Yin, S. Y. Xu, Y. Zhang, D. T. Xie, Z. L. Li, *Electrochim. Acta* **2016,** *191*, 743-749.
[113] G. Yang, L. Huang, Z. Yu, X. Liu, S. Chen, J. Zeng, S. Zhou, L. Zhuang, *Water Res.* **2019,** *159*, 294-301.

[114] R. E. Zeebe, D. Wolf-Gladrow, Chapter 2. Kinetics. In *CO_2 in Seawater: Equilibrium, Kinetics, Isotopes*, 3rd ed.; Halpern, D., Ed. Elsevier Science: San Diego, USA, 2005.
[115] H. Yi, K. P. Nevin, B. C. Kim, A. E. Franks, A. Klimes, L. M. Tender, D. R. Lovley, *Biosens. Bioelectron* **2009,** *24*, 3498-3503.
[116] X. Zhang, J. Philips, H. Roume, K. Guo, K. Rabaey, A. Prévoteau, *ChemElectroChem* **2017,** *4*, 1026-1036.
[117] C. Shu, Q. Zhu, K. Xiao, Y. Hou, H. Ma, J. Ma, X. Sun, *BioMed Res. Int.* **2019,** *2019*, 6151587.
[118] K. P. Katuri, S. Rengaraj, P. Kavanagh, V. O'Flaherty, D. Leech, *Langmuir* **2012,** *28*, 7904-7913.
[119] N. F. Polizzi, S. S. Skourtis, D. N. Beratan, *Faraday Discuss.* **2012,** *155*, 43-61.
[120] B. R. Dhar, H. Ryu, H. Ren, J. W. S. Domingo, J. Chae, H. S. Lee, *ChemSusChem* **2016,** *9*, 3485-3491.

Entry for the Table of Contents

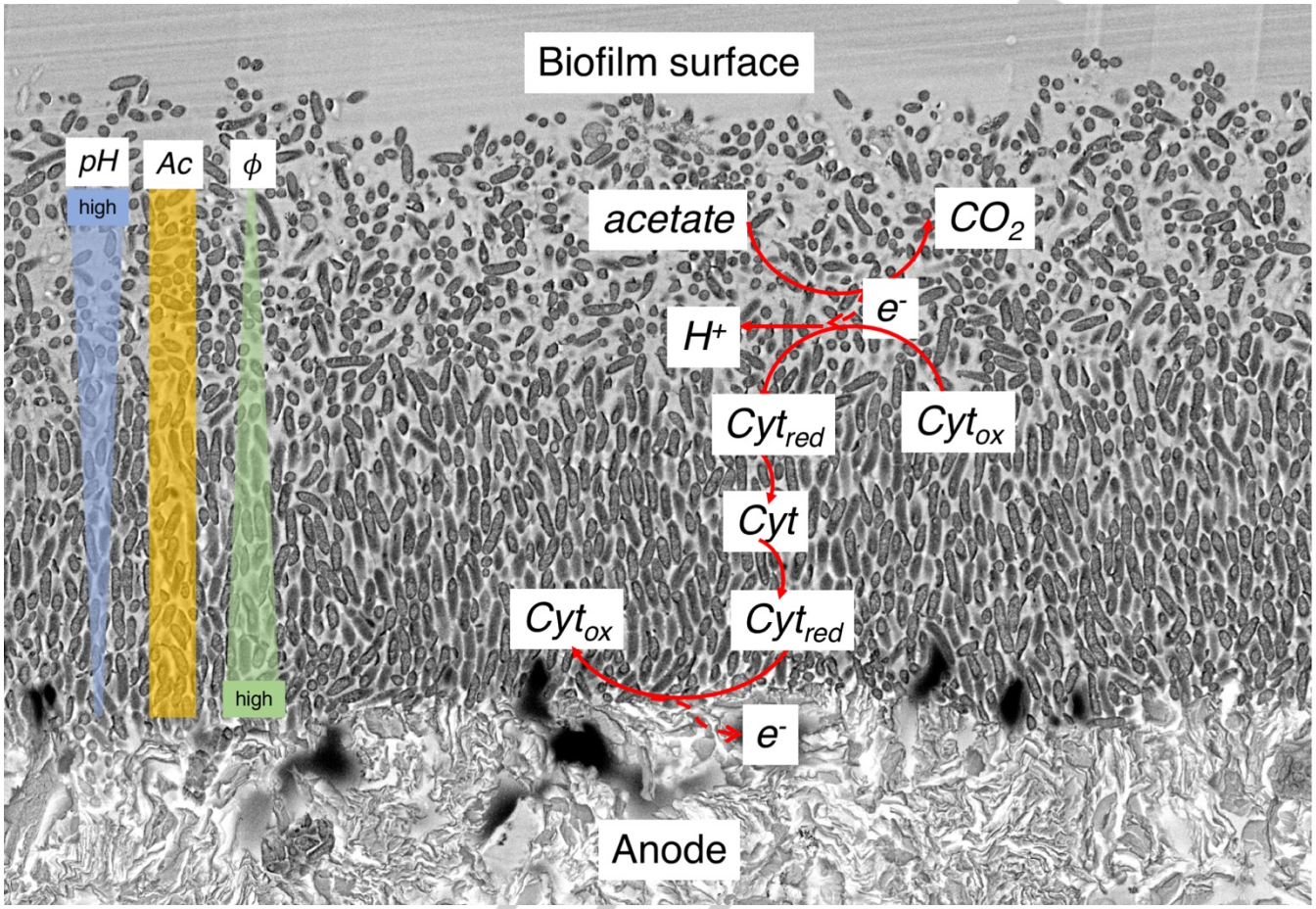

Direct extracellular electron transfer from *Gebacter sulfurreducens* biofilms to terminal electrode is carried out via a chain of redox active molecules (e.g. cytochromes). The proposed model provides a theoretical framework describing this direct electron transfer process and is experimentally validated using stable isotope (^{15}N) probing with nanoSIMS. Symbols in this figure: ϕ-electric potential, Ac-acetate, Cyt_{ox} and Cyt_{red} are oxidized and reduced cytochromes, respectively.

Institute and/or researcher Twitter usernames: ((optional))